




Current-induced dynamics of isolated antiferromagnetic antiskyrmion and antiskyrmionium

Shuang Li ¹, Motohiko Ezawa ², and Yan Zhou ^{1,*}

¹*School of Science and Engineering, The Chinese University of Hong Kong, Shenzhen, Guangdong 518172, China*

²*Department of Applied Physics, The University of Tokyo, 7-3-1 Hongo, Tokyo 113-8656, Japan*



(Received 5 January 2023; revised 1 April 2023; accepted 26 April 2023; published 9 May 2023)

Topologically stable spin structures known as magnetic antiskyrmions spontaneously emerge in magnets with broken in-plane rotation symmetry when current is injected. While many studies have focused on their behaviors in ferromagnetic (FM) materials, limited attention has been paid to antiskyrmions in their antiferromagnetic (AFM) counterparts. In spintronic applications, the Magnus force of an AFM antiskyrmion cancels out completely due to its comparable but opposite sign spin pattern on the A and B sublattices in the AFM bipartite system, while an FM antiskyrmion exhibits transverse motion when driven by the currents, causing limitations to antiskyrmion motion velocity and information loss when the antiskyrmion is annihilated at the edges of racetracks. Here, we report the nucleation and dynamics of an isolated AFM antiskyrmion and antiskyrmionium induced by current analytically and numerically. We demonstrate how AFM antiskyrmions and antiskyrmioniums are stabilized and manipulated with the same velocity by spin transfer torques and with different velocities by spin-orbit torques. Under suitable conditions, the AFM antiskyrmion and antiskyrmionium can be driven at velocities as high as 6 km/s without the skyrmion Hall effect, far greater than their ferromagnetic counterparts. Furthermore, the critical driving current density of the AFM antiskyrmion (antiskyrmionium) is much larger than that of the FM antiskyrmion (antiskyrmionium). Our results contribute to the development of antiferromagnetic antiskyrmions and antiskyrmioniums by shedding light on their stabilization and dynamics.

DOI: [10.1103/PhysRevB.107.174409](https://doi.org/10.1103/PhysRevB.107.174409)

I. INTRODUCTION

Magnetic skyrmions and antiskyrmions are topologically protected spin-whirling structures that have been the subject of intense research due to their emerging properties and prospective spintronics applications as nonvolatile information carrier candidates [1–9]. They are usually stabilized by the Dzyaloshinskii-Moriya interaction (DMI) [10,11], resulting from the spin-orbit interaction and broken structure-inversion symmetry. Magnetic skyrmions have been investigated theoretically [1–5] and experimentally [12–16] in isotropic systems with the same sign ($D_x = D_y$) for the DMI, where D_x and D_y are DMI strengths along two perpendicular directions. However, magnetic antiskyrmions, which differ from isotropic chiral skyrmions, exist in anisotropic materials with opposite DMI signs ($D_x = -D_y$) [17–30]. Magnetic antiskyrmions offer some advantages over magnetic skyrmions because they can be driven without the Hall-like motion at a critical current direction [17] and offer increased stability due to dipolar interactions [18]. Furthermore, recent experiments have shown that metastable antiskyrmions can be transformed into skyrmions or nontopological bubbles by tuning the magnitude and direction of the external magnetic field [19,20]. Antiskyrmions have negative topological charges and can be seen as the antimatter of skyrmions. Therefore, studying these structures is both interesting and important for advancing our understanding of topological spin structures.

Magnetic antiskyrmions are experimentally observed in tetragonal Heusler materials with D_{2d} crystal symmetry above room temperature [20–22] and $\text{Fe}_{1.9}\text{Ni}_{0.9}\text{Pd}_{0.2}\text{P}$ magnets with S_4 symmetry [19,23,24]. They are also theoretically investigated in thin-film systems [17,18,31] and frustrated systems [32–35]. The creation of the ferromagnetic (FM) antiskyrmion [36–39], stabilization in the presence of anisotropic DMI [17,28,30,40], and dynamics induced by the current [17], magnetic field [41], and microwave electric field [42] have been explored. However, the dynamics of FM antiskyrmions exhibits the same drawbacks as the FM skyrmions, namely, the skyrmion Hall effect [14,17,43], which may lead to information loss in spintronic applications. One approach to get around it is to create a ferromagnetically coupled skyrmion-antiskyrmion bilayer using currents [9,17,44], which could lead to a vanishing total Magnus force since the skyrmion has topological charge $Q = +1$ and the antiskyrmion has topological charge $Q = -1$. Additionally, simulations show that the FM antiskyrmionium, which is composed of two coaxial antiskyrmions with opposite topological charges, has no skyrmion Hall effect [45].

Another effective way, inspired by the concepts of antiferromagnetic (AFM) skyrmions [46–48] and bilayer skyrmions [49] via antiferromagnetic coupling, is to host the antiskyrmions in antiferromagnets. In an AFM system with a bipartite lattice, the topological charges in the two sublattices cancel out, thus making the spin textures free from the skyrmion Hall effect [50–54]. Previous reports indicate that the AFM antiskyrmions may exist in tetragonal antiferromagnets like $\text{Ba}_2\text{CuGe}_2\text{O}_7$ [55–57] of the class D_{2d} and $\text{K}_2\text{V}_3\text{O}_8$

*zhouyan@cuhk.edu.cn

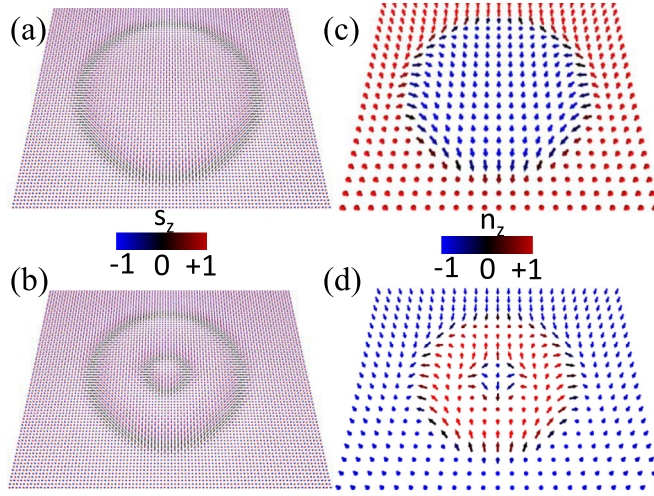


FIG. 1. Structures of an AFM (a) antiskyrmion and (b) antiskyrmionium in real space. The arrows indicate the spin vectors. The zoomed-in Néel vector components n_z of the (c) antiskyrmion and (d) antiskyrmionium.

[55,58] of the class C_{4v} . Simultaneously, hybrid Monte Carlo simulations demonstrate that the FM skyrmions and the FM antiskyrmions can be converted into their AFM counterparts via interface engineering at the interface between an AFM insulator and a spin-orbit coupled metal [59]. Although magnetic antiskyrmions in FM systems have received a lot of attention, there is still much to learn about their counterparts in AFM materials [55,59], which is also important for developing spintronic applications.

In this work, we focus on the creation, stabilization, and current-driven dynamics of AFM antiskyrmions [Fig. 1(a)] and antiskyrmioniums [Fig. 1(b)]. We propose a method for creating an AFM antiskyrmion and an antiskyrmionium in a designed geometry using the spin current and analyze their dynamics analytically and numerically. We find that the AFM antiskyrmion and the AFM antiskyrmionium have the same velocities when driven by spin transfer torques, but their steady motion velocities differ when driven by spin-orbit torques. Unlike the FM antiskyrmion, the AFM antiskyrmion moves along the racetrack without transverse motion. When the applied current is strong, the AFM antiskyrmionium is stabler and difficult to deform compared to the FM antiskyrmionium. Furthermore, we study the dynamics of antiferromagnetically coupled bilayer antiskyrmions driven by current, where the Magnus force in the bilayer can be canceled.

II. MODEL AND SIMULATION

We consider a G -type AFM film with anisotropic DMI and perpendicular magnetic anisotropy. From the classical Heisenberg Hamiltonian, the energy of the AFM system E can be written in the following continuous form [46,60]:

$$E = \int dV \frac{\lambda}{2} \mathbf{m}^2 + \frac{A}{2} [(\nabla \mathbf{n})^2 + \partial_x \mathbf{n} \cdot \partial_y \mathbf{n}] + L \mathbf{m} \cdot (\partial_x \mathbf{n} + \partial_y \mathbf{n}) + \frac{K}{2} (1 - n_z^2) + w_D, \quad (1)$$

where λ , A , L , and K are the homogeneous exchange constant, inhomogeneous exchange constant, parity-breaking constant, and magnetic anisotropy constant, respectively [60]. The effect of the dipolar interactions is negligible in AFM systems in general because the spin is antiparallel. The staggered magnetization or the Néel vector [60,61] and the total magnetization are defined as

$$\mathbf{n} = (\mathbf{s}_{i+1,j}^A - \mathbf{s}_{i,j}^B)/2, \quad \mathbf{m} = (\mathbf{s}_{i+1,j}^A + \mathbf{s}_{i,j}^B)/2, \quad (2)$$

where $\mathbf{s}_{i,j}^\tau$ is the unit magnetic moment with sublattice parameters $\tau = A, B$ and sublattice site (i, j) . For the antiferromagnets under consideration, the Lifshitz invariants quartic in the components of \mathbf{n} have the following formats [55]:

$$\text{class } D_{2d} : w_D = D_x(n_z \partial_x n_y - n_y \partial_x n_z) + D_y(n_z \partial_y n_x - n_x \partial_y n_z), \quad (3a)$$

$$\text{class } C_{nv} : w_D = D_x(n_z \partial_x n_x - n_x \partial_x n_z) + D_y(n_z \partial_y n_y - n_y \partial_y n_z). \quad (3b)$$

Class D_{2d} is employed to stabilize the Bloch-type antiskyrmion and antiskyrmionium, while class C_{nv} stabilizes the Néel-type antiskyrmion and antiskyrmionium. Here, we adopt the C_{nv} symmetry class, stabilizing the structures and typical AFM parameters for simulations with modified MUMAX3 software including the negative exchange constant [50,53] and the anisotropic DMI [62]: the saturation magnetization $M_s = 3.76 \times 10^5 \text{ A m}^{-1}$, the exchange stiffness $A = -6.59 \times 10^{-12} \text{ J m}^{-1}$, the PMA constant $K = 0.6 \times 10^6 \text{ J m}^{-3}$, and the Gilbert damping constant $\alpha = 0.1$. The lattice constant is 0.5 nm .

For the spin dynamics driven by spin torques, the Néel vector \mathbf{n} and the total magnetization \mathbf{m} obey the following coupled equations [61]:

$$\dot{\mathbf{n}} = (\gamma \mathbf{f}_m - \alpha \dot{\mathbf{m}}) \times \mathbf{n} + \mathbf{T}_{n,\text{SOT}} + \mathbf{T}_{n,\text{STT}}, \quad (4a)$$

$$\dot{\mathbf{m}} = (\gamma \mathbf{f}_n - \alpha \dot{\mathbf{n}}) \times \mathbf{n} + \mathbf{T}_{nl} + \mathbf{T}_{m,\text{SOT}} + \mathbf{T}_{m,\text{STT}}, \quad (4b)$$

where γ and α are the gyromagnetic ratio and damping constant. In the derivation process, we disregard all nonlinear terms that are contained in \mathbf{T}_{nl} [61]. $\mathbf{f}_m = -\delta E / (\mu_0 M_s \delta \mathbf{m})$ and $\mathbf{f}_n = -\delta E / (\mu_0 M_s \delta \mathbf{n})$ are the effective fields. $\mathbf{T}_{n,\text{SOT}} = \gamma H_d \mathbf{m} \times \mathbf{p} \times \mathbf{n}$ and $\mathbf{T}_{m,\text{SOT}} = \gamma H_d \mathbf{n} \times \mathbf{p} \times \mathbf{n}$ are damping-like spin-orbit torques (SOTs), where we assume that the polarization $\mathbf{p} = -\hat{\mathbf{e}}_y$, which is determined by the spin Hall effect in the substrate, and $H_d = j \hbar \theta_{\text{SH}} / (2 \mu_0 e M_s t_z)$, with \hbar being the reduced Planck constant, θ_{SH} being the spin Hall angle, μ_0 being the vacuum permeability constant, e being the elementary charge, and t_z being the AFM layer thickness. $\mathbf{T}_{n,\text{STT}} = \gamma \eta (\mathbf{J} \cdot \nabla) \mathbf{n}$ and $\mathbf{T}_{m,\text{STT}} = \gamma \beta (\mathbf{J} \cdot \nabla) \mathbf{n} \times \mathbf{n}$ are spin transfer torques (STTs) with current density j . The current is applied along the x axis to drive the AFM antiskyrmion and antiskyrmionium. The adiabatic parameter $\eta = \beta / \xi$ and nonadiabatic parameter $\beta = \mu_B P \xi / [e \gamma M_s (1 + \xi^2)]$, with polarization $P = 0.4$ and $\xi = 0.2$, are adopted in the following simulations.

Substituting

$$\mathbf{f}_m = -\frac{\lambda}{\mu_0 M_s} \mathbf{m} - \frac{L}{\mu_0 M_s} (\partial_x \mathbf{n} + \partial_y \mathbf{n}) \quad (5)$$

into Eq. (4a), where only the leading terms are kept, the net magnetization \mathbf{m} is obtained as

$$\mathbf{m} = \frac{\mu_0 M_s}{\gamma \lambda} \dot{\mathbf{n}} \times \mathbf{n} - \frac{L}{\lambda} (\partial_x \mathbf{n} + \partial_y \mathbf{n}) - \frac{\alpha \mu_0 M_s}{\lambda} \mathbf{f}_n \times \mathbf{n}. \quad (6)$$

The last damping term can be ignored because it is weak [61]. Combining Eqs. (6) and (4b), we find

$$\begin{aligned} \frac{\mu_0 M_s}{\gamma \lambda} \ddot{\mathbf{n}} \times \mathbf{n} - \frac{L}{\lambda} \partial_t \dot{\mathbf{n}} &= \gamma \mathbf{f}_n^* \times \mathbf{n} - \alpha \dot{\mathbf{n}} \times \mathbf{n} \\ &+ \gamma H_d \mathbf{n} \times \mathbf{p} \times \mathbf{n} + \gamma \beta j \partial_x \mathbf{n} \times \mathbf{n}, \end{aligned} \quad (7)$$

where

$$\begin{aligned} \mathbf{f}_n^* &= \frac{A^*}{\mu_0 M_s} (\partial_{xx} + \partial_{yy}) \mathbf{n} + \frac{K}{\mu_0 M_s} n_z \mathbf{e}_z \\ &+ \frac{D}{\mu_0 M_s} [\partial_x n_z \mathbf{e}_x + \partial_y n_z \mathbf{e}_y - (\partial_x n_x + \partial_y n_y) \mathbf{e}_z], \end{aligned} \quad (8)$$

with $A^* = A/2$ and $D_x = -D_y = D$.

Using the scalar product in Eq. (7) with $\mu_0 M_s \partial_t \mathbf{n}$ and integrating over the space, the Thiele equation [46,60,63,64] is written as

$$\mathbf{a} \cdot \mathbf{M}_{\text{eff}} = \mathbf{F}_\alpha + \mathbf{F}_{\text{SOT}} + \mathbf{F}_{\text{STT}}, \quad (9)$$

where \mathbf{a} is the acceleration and \mathbf{M}_{eff} is the effective mass, which is defined as $\mu_0^2 M_s^2 t_z \mathbf{D} / \gamma^2 \lambda$ [46,61]. The first term on the right side is the dissipative force,

$$\mathbf{F}_\alpha = -\alpha \mu_0 M_s t_z \mathbf{v} \cdot \mathbf{D} / \gamma, \quad (10)$$

where the dissipative tensor \mathbf{D} is given by $\mathbf{D} = \begin{pmatrix} d_{xx} & d_{xy} \\ d_{yx} & d_{yy} \end{pmatrix}$, with $d_{ij} = \delta_{ij} d = \int dx dy (\partial_i \mathbf{n} \cdot \partial_j \mathbf{n})$. The second term is the force induced by the SOT,

$$\mathbf{F}_{\text{SOT}} = -\mu_0 H_d M_s t_z (u_x \mathbf{e}_x + u_y \mathbf{e}_y), \quad (11)$$

with $u_i = \int dx dy [(\mathbf{n} \times \mathbf{p}) \cdot \partial_i \mathbf{n}]$. The third term is the STT force,

$$\mathbf{F}_{\text{STT}} = -\mu_0 M_s t_z \beta j d \mathbf{e}_x. \quad (12)$$

The components of the dissipation tensor \mathbf{D} and the vector \mathbf{u} are determined by the spin configurations described by $\mathbf{n} = [\sin \theta(r) \cos \phi(\varphi), \sin \theta(r) \sin \phi(\varphi), \cos \theta(r)]$ in polar coordinates (r, φ) , as shown in the Appendix.

For the steady motion of an AFM antiskyrmion (antiskyrmionium), the acceleration equals zero, and the steady motion speed is given by the following matrix:

$$\begin{pmatrix} v_x \\ v_y \end{pmatrix} = \frac{\gamma H_d}{\alpha d} \begin{pmatrix} u_x \\ u_y \end{pmatrix} + \frac{\gamma \beta j}{\alpha} \begin{pmatrix} e_x \\ 0 \end{pmatrix}. \quad (13)$$

The first term on the right-hand side corresponds to the velocity induced by the SOTs, while the second term on the right-hand side corresponds to the velocity induced by the STTs. A detailed derivation is shown in the Appendix.

III. CREATION OF AN AFM ANTISKYRMION AND ANTISKYRMIONIUM

We discuss a method to nucleate an AFM antiskyrmion and antiskyrmionium in a thin magnetic film. Such a process

necessarily involves overcoming the topological barrier. Motivated by the creation of an FM antiskyrmionium [45], we performed micromagnetic simulations on the designed geometry depicted in Fig. 2(a), which consisted of a magnetic film ($300 \times 300 \times 0.5 \text{ nm}^3$) with four adjacent circles (radius 17 nm) for the injection of a vertical current with the spin polarized along the $-z$ direction and a polarization rate of 0.4. The system was relaxed after the application of the spin current pulse, which was applied for 30 ps. The current injection area is designed in this way because it can confine the flipping of the spins, and the spins at the boundary of the area can be connected together to form magnetic domains.

The spins are flipped in the confined circles after the application of spin current, which results in domain walls. For nucleation of the AFM antiskyrmion, the current pulse is $1 \times 10^{15} \text{ A m}^{-2}$, and the distance l between the centers of any two nonadjacent circles is 40 nm. After the spin current is applied, the outer domain walls get connected to each other in the specially designed intersect circles [Fig. 2(b)]. When the spin current pulse is turned off, the magnetic domain walls first evolve into a deformed antiskyrmion, which contains two small deformed antiskyrmions [Fig. 2(c)]. The two small antiskyrmions are unstable and then disappear. The big antiskyrmion gradually evolves into an isolated stable antiskyrmion as shown in Fig. 2(d). Because of the anisotropic DMI, the spin directions in the x direction are the inverse of those in the y direction. This anisotropic DMI configuration favors opposite chirality along the x and y axes, allowing the AFM antiskyrmion to be stable [55]. For nucleation of the AFM antiskyrmionium, the same method and model can be used. With $j = 1 \times 10^{15} \text{ A m}^{-2}$ and separation $l = 42 \text{ nm}$, the outer and inner domain walls are formed and get connected around the outer and inner circles after the spin current is applied [Fig. 2(e)]. The connected domain walls transform into a deformed antiskyrmionium, as shown in Fig. 2(f) when the spin current is off. Figure 2(g) shows an isolated stable antiskyrmionium after the relaxation. The detailed creation processes are shown in the movies in the Supplemental Material [65].

The time evolution of the topological charges of the AFM system is represented in Fig. 2(h). In our numerical computation, we employ the discrete version of the topological number for each sublattice ($\tau = A, B$) [48],

$$Q_\tau = -(1/4\pi) \sum_{(i,j,k)} \mathbf{s}_i^\tau \cdot (\mathbf{s}_j^\tau \times \mathbf{s}_k^\tau). \quad (14)$$

A set of two topological numbers (Q_A, Q_B) is assigned to an AFM system. We obtain $Q_A = -Q_B$ in general. Here, we choose $Q = -Q_B$ to be the topological number so that $Q = -1$ for an antiskyrmion. Due to the contribution from the tilted spins at the edges, the AFM background state is not equal to zero. The topological number changes as the spin current is injected. For the relaxation process of the AFM antiskyrmion, the topological number changes to 2.5 sharply because three deformed antiskyrmions are created and the center magnetizations of these three antiskyrmions are reversed and then changes to -1 , corresponding to the annihilation of two inner antiskyrmions and the reversal of the big antiskyrmion. In the relaxation process of the AFM

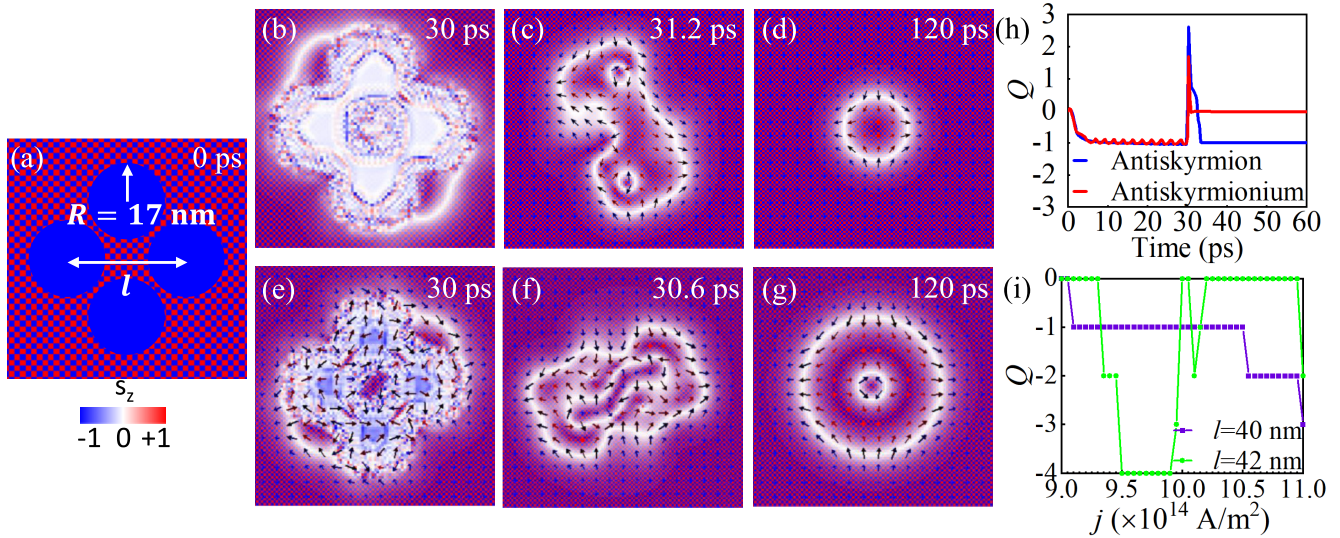


FIG. 2. The creation process of an AFM antiskyrmion and an antiskyrmionium. (a) Schematic of contact pads for nucleating an isolated AFM antiskyrmion and antiskyrmionium. The four blue circles are the connected pads with a $\mathbf{p} = -\mathbf{e}_z$ spin current. The color bar shows the z components of magnetization. (b)–(d) Inversion of magnetization in the creation process of an AFM antiskyrmion when $j = 1 \times 10^{15} \text{ A m}^{-2}$ and $l = 40 \text{ nm}$. (e)–(g) Inversion of magnetization in the creation process of an AFM antiskyrmionium when $j = 1 \times 10^{15} \text{ A m}^{-2}$ and $l = 42 \text{ nm}$. Arrows show the projection of magnetization on the plane. Here, we use $D_x = -D_y = 3.4 \text{ mJ m}^{-2}$. (h) The time involution of the topological number Q in the creation process of an AFM antiskyrmion ($j = 1 \times 10^{15} \text{ A m}^{-2}$ and $l = 40 \text{ nm}$) and antiskyrmionium ($j = 1 \times 10^{15} \text{ A m}^{-2}$ and $l = 42 \text{ nm}$). (i) The topological number Q of the final relaxed state under different current densities j and distances l .

antiskyrmionium, singularities appear at 30 ps, and a topological transition occurs. The system then relaxes to a stable structure, with the topological number remaining stable at zero. Figure 2(i) shows the topological number of the relaxed states under different current densities and geometries. At low current density ($j = 9 \times 10^{14} \text{ A m}^{-2}$), the current is not enough to break the AFM-exchange interactions, resulting in a relaxed AFM state. When the distance l is small (40 nm), an antiskyrmion is nucleated, and the number of antiskyrmions increases with the current. Multiple antiskyrmions are nucleated at low current density when $l = 42 \text{ nm}$. As the current increases, the inner domain walls are formed, and an antiskyrmionium is nucleated. However, the inner domain walls are annihilated at high current density, resulting in the system relaxing to multiple antiskyrmions again.

IV. STABILIZATION OF AN AFM ANTISKYRMION AND ANTISKYRMIONIUM

We study the stability of an AFM antiskyrmion and an AFM antiskyrmionium in nanodisks in the presence of the anisotropic interface DMI. We numerically determined relaxed micromagnetic states of 150 nm wide, 0.5 nm thick nanodisks for various DMI constants D_x and initial states.

Anisotropic DMI was observed at the Co/W(110) interface, where it was discovered that the Dzyaloshinskii-Moriya vector strength had the same sign but was 2.5 times stronger in magnitude along the $\text{bcc}[1\bar{1}0]$ direction than the orthogonal direction $\text{bcc}[001]$ [29]. The geometry of spin configurations is elliptical when D_x and D_y are not identical in magnitude, which influences the skyrmion or antiskyrmion Hall angle [66]. However, we assume that the Dzyaloshinskii-Moriya

constants have the same magnitude but opposite signs, i.e., $D_x = -D_y$, for the sake of simplicity.

We first construct the initial spin configurations corresponding to the AFM state, the AFM antiskyrmion, and the AFM antiskyrmionium and then relax the systems to the final states in order to determine the total energy. Figure 3 shows the total micromagnetic energy of three possible configurations as a function of D_x . Actually, an AFM ground state is not uniform at the boundaries, and hence, the energy depends on D_x , as shown in Fig. 3. The energy of the AFM state decreases with increasing D_x .

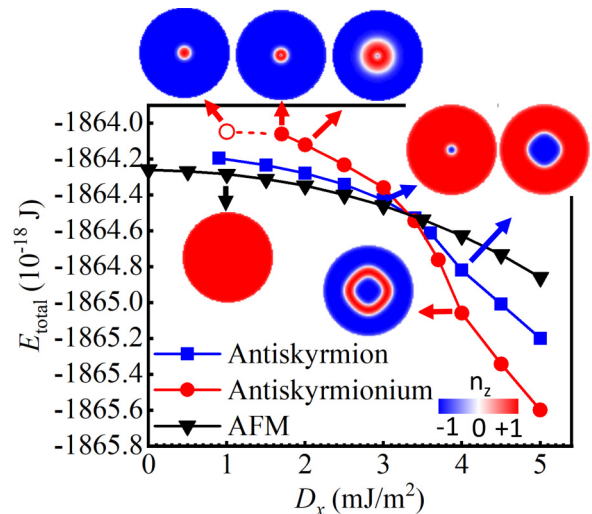


FIG. 3. Total micromagnetic energy of the AFM state, the AFM antiskyrmion, and the AFM antiskyrmionium in a nanodisk as a function of D_x ($D_x = -D_y$). The insets show examples of relaxed Néel vector distributions for several points on the graph.

Starting with an initial AFM antiskyrmion state, we find that across a large range of D_x , the relaxed stable state is always an AFM antiskyrmion state, with the AFM antiskyrmion size increasing with D_x . At large values of the DMI, the anisotropy becomes stronger, resulting in an asymmetrical shape. The Néel vector profiles of several points are plotted. The DMI energy is reduced by an inward tilt of the spins, leading to a drop in energy with D_x .

On the other hand, starting from an initial AFM antiskyrmionium state, the relaxed state is not an AFM antiskyrmionium state but an AFM antiskyrmion state for $D_x < 1.7 \text{ mJ m}^{-2}$, while the relaxed state is an AFM antiskyrmionium for D_x in the range $1.7\text{--}5 \text{ mJ m}^{-2}$. When $D_x = 3.4 \text{ mJ m}^{-2}$, the energies of the AFM antiskyrmion state and the AFM antiskyrmionium state are degenerate. The ground state in thin film with perpendicular magnetic anisotropy is cycloidal, depending not only on the DMI strength but also on the dimensions of the film [17,46,67,68]. The AFM antiskyrmion (antiskyrmionium) is confined in the nanodisk, which limits the increase in diameter. For $D_x < 3.4 \text{ mJ m}^{-2}$, the diameter of the AFM antiskyrmion is not too large compared to the nanodisk, and it is stabler. However, for $D_x > 3.4 \text{ mJ m}^{-2}$, the expansion of the AFM antiskyrmion is limited, with the spins rotating by 2π from the center to the edge of the nanodisk. Consequently, the AFM antiskyrmionium becomes stabler [67]. These results indicate that it is possible to create stable or metastable AFM antiskyrms and antiskyrmioniums in nanodisks with different values of the material parameters.

V. THE CURRENT-DRIVEN MOTION OF AFM ANTISKYRMIONS AND ANTISKYRMIONIUMS

In this section, we compare the current-induced dynamical properties of the AFM antiskyrmion and the AFM antiskyrmionium. Using the same nonadiabatic parameter and damping constant, Eq. (13) leads to identical motion velocities for the AFM antiskyrmion and the AFM antiskyrmionium driven by the STTs. However, the AFM antiskyrmion and the AFM antiskyrmionium experience different results depending on the magnetic configurations for SOT-induced steady motion. We simulate the motion of the AFM antiskyrmion and antiskyrmionium to validate the above analytical results, where the relaxed states are the corresponding AFM antiskyrmion and antiskyrmionium. The numerical velocities are calculated as

$$\mathbf{v} \equiv (v_x, v_y) = (\dot{r}_x, \dot{r}_y), \quad (15)$$

where the guiding center (r_x, r_y) is used to track the position of the AFM antiskyrmion and antiskyrmionium, which are defined by

$$r_i = \frac{\int \mathbf{i} \mathbf{n} \cdot (\partial_x \mathbf{n} \times \partial_y \mathbf{n}) dx dy}{\int \mathbf{n} \cdot (\partial_x \mathbf{n} \times \partial_y \mathbf{n}) dx dy}, \quad i = x, y, \quad (16)$$

for the AFM antiskyrmion and

$$r_i = \int i(1 - n_z) dx dy / \int (1 - n_z) dx dy, \quad i = x, y, \quad (17)$$

for the AFM antiskyrmionium [46,69].

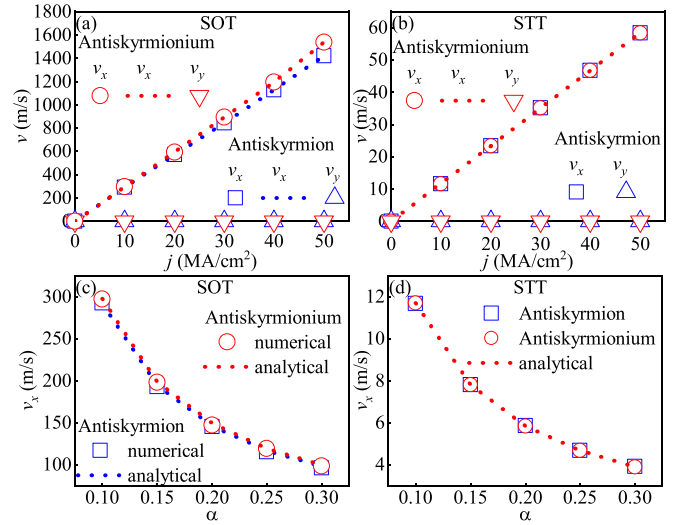


FIG. 4. The velocities of the AFM antiskyrmion and the AFM antiskyrmionium as a function of the current densities and the damping constants induced by the SOT and the STT. The damping constant $\alpha = 0.1$ in (a) and (b), and the current is 10 MA cm^{-2} in (c) and (d). Symbols represent the results from numerical simulations, and the dotted lines indicate the analytical results.

Figures 4(a) and 4(b) show the velocities of the AFM antiskyrmion and antiskyrmionium driven by the SOT and the STT, respectively. When the STT is considered, it is seen that the y component of the velocity for both the AFM antiskyrmion and antiskyrmionium is zero and the x component of the velocity increases with the current density j and decreases with the damping constant α , as shown in Figs. 4(b) and 4(d), which are in good agreement with the motion governed by Eq. (13). Regarding the SOT, the x components of the velocity of the antiskyrmion and antiskyrmionium show a similar increasing tendency with increasing current density [Fig. 4(a)] and decreasing damping constant [Fig. 4(c)], with the y component remaining zero. According to Eq. (13), the y component of the velocity for the SOT depends on the dissipative tensor \mathbf{D} and the vector \mathbf{u} . The Appendix confirms that the y component of the vector \mathbf{u} is zero. However, the x components of the velocities of the antiskyrmion and antiskyrmionium are different, and the difference increases with the current. This result is consistent with the AFM skyrmion and antiskyrmionium [46]. It has been found that the skyrmions and antiskyrmions in FM systems have the same velocities. When the skyrmions and antiskyrmions are driven by the currents, a transverse motion arises due to the Magnus force associated with the topological charge. The FM antiskyrmion Hall angle strongly depends on the direction of the applied current with respect to the in-plane spin structures of the antiskyrmion [17]. In contrast, they do not exhibit the skyrmion Hall effect in AFM systems, resulting in no difference in the dynamics between AFM skyrmions and antiskyrmions. As in the case of the skyrmionium and antiskyrmionium in FM systems, they both move along the current with the same velocity when induced by the STTs. When the SOT is taken into account, the skyrmionium moves along the current, while the antiskyrmionium deviates from the current because of anisotropic magnetization distribution [45]. This deviation

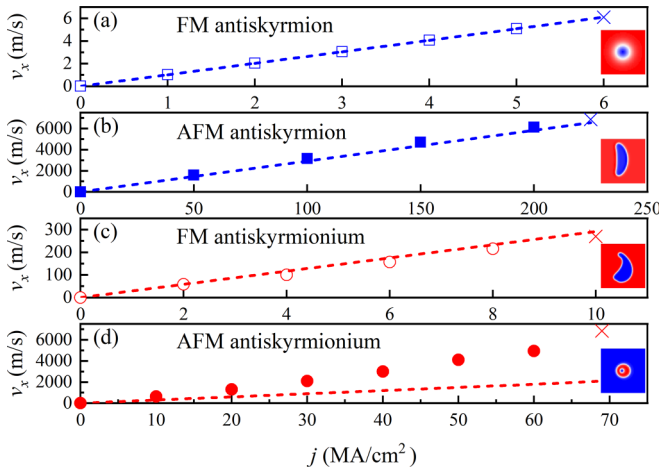


FIG. 5. Comparison between the current-induced dynamics of (a) the FM antiskyrmion, (b) the AFM antiskyrmion, (c) the FM antiskyrmionium, and (d) the AFM antiskyrmionium. The insets show the top views of spin configurations at critical current densities, which are indicated by crosses. Symbols represent the results from numerical simulations, and the dashed lines indicate the analytical results. The values of u/d are 4.72 and 4.83 nm for the antiskyrmion and antiskyrmionium, respectively.

disappears in AFM systems due to antiparallel magnetization. To further explore the dynamical properties of the AFM antiskyrmion and antiskyrmionium, we compare the current-induced dynamics of the antiskyrmion and antiskyrmionium in different magnetic systems. From the above results, SOT is more efficient in driving both the AFM antiskyrmion and antiskyrmionium, so we just consider SOT-induced motion in both FM and AFM systems.

Figure 5(a) shows that the threshold current for the FM antiskyrmion is 6 MA cm^{-2} . When the current is larger than this value, the FM antiskyrmion moves to the edge resulting from the Magnus force and is finally annihilated by touching the edge. Compared with the FM antiskyrmion, the AFM antiskyrmion can move along the racetrack without deflection due to a complete cancellation of the Magnus force. However, the AFM antiskyrmion gets elongated along the axis perpendicular to the direction of propagation as the velocity increases, as shown in the inset in Fig. 5(b). Previous studies have also observed the elliptical deformations and breakdown in traveling of the AFM skyrmions, which arises from a local imbalance of gyrotropic forces [70–73], and the critical velocity of the deformation and breakdown depends strongly on the material parameters and is defined by [70]

$$v_c = \sqrt{\left(1 - \frac{\pi^2 D^2}{16AK}\right) \frac{\gamma A a^2}{2M_s}}, \quad (18)$$

where a is the lattice constant.

The critical velocity for the AFM structures in our model is 6892.8 m s^{-1} , calculated from Eq. (18). Beyond this value, they will elongate indefinitely until reaching the width of the racetrack. Figure 5(b) shows that the AFM antiskyrmion approximately approaches the critical velocity 6853 m s^{-1} when the current density is 225 MA cm^{-2} . For the destruction of the FM antiskyrmionium in Fig. 5(c), the FM antiskyrmio-

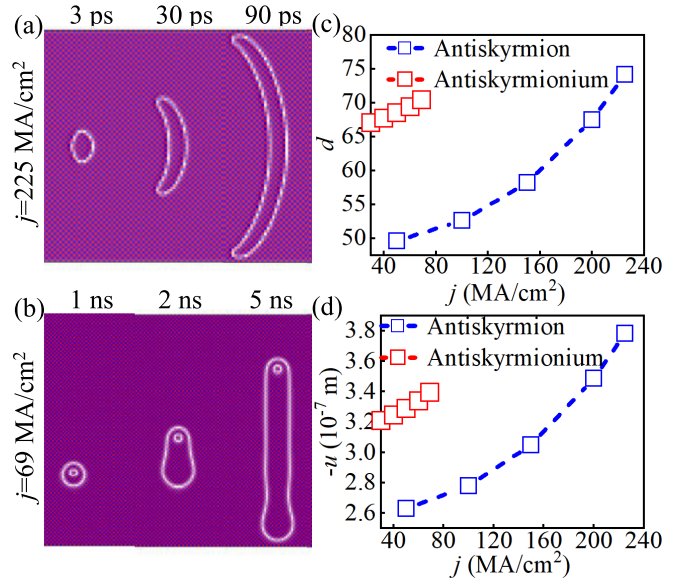


FIG. 6. Intermediate magnetization profiles of a traveling (a) AFM antiskyrmion at 225 MA cm^{-2} and (b) AFM antiskyrmionium at 69 MA cm^{-2} . The components of (c) the dissipative tensor \mathbf{D} and (d) vector \mathbf{u} as a function of the current densities at $t = 6 \text{ ps}$, showing varying degrees of dynamic deformation.

nium is destroyed into an antiskyrmion when the driving current density is 10 MA cm^{-2} since opposite Magnus forces act on the inner and outer antiskyrmions, with the inner antiskyrmion shrinking and the outer antiskyrmion expanding [74]. On the other hand, the critical driving current density where the AFM antiskyrmionium moves at the critical velocity is 69 MA cm^{-2} , as shown in Fig. 5(d), which is larger than that for the destruction of the FM antiskyrmionium. The distorted motion of the AFM antiskyrmionium can cause the components of the tensor \mathbf{D} and vector \mathbf{u} to deviate from their constant values, leading to velocities that differ from the analytical solutions. Figures 5(c) and 5(d) show that the deviation is larger for the AFM antiskyrmionium in comparison to the FM antiskyrmionium. For the FM antiskyrmionium, the inner antiskyrmion is annihilated at relatively lower current because of the opposite gyroscopic force, where the shape of the antiskyrmionium does not change dramatically. However, the AFM antiskyrmionium shows severe distortion at higher current, while the inner antiskyrmion still remains stable. When the microstructures of the FM and AFM systems are compared, it can be shown that the antiferromagnetically coupled pair of sublattices in the AFM system has the same magnetic spins and gyromagnetic ratio, which entirely cancels the net angular momentum [75]. The gyroscopic force acting on each antiskyrmion in the FM system, however, rises proportionally to the current density since the antiskyrmionium is a composite structure comprising two antiskyrmions with opposite chiralities. At the larger current densities, this growing gyroscopic force causes the antiskyrmionium deformation.

We now discuss the deformations of the AFM antiskyrmion and antiskyrmionium. Figures 6(a) and 6(b) show the intermediate snapshots of the traveling AFM antiskyrmion and antiskyrmionium at their respective critical current densities. Both structures become elliptical in shape. Accelerating

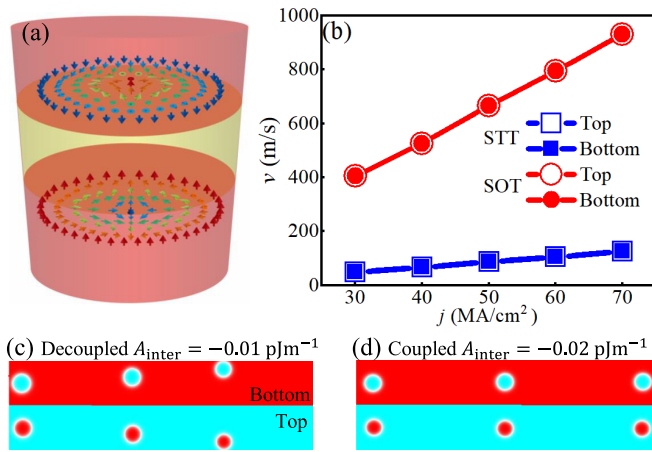


FIG. 7. Current-induced motion of antiferromagnetically coupled bilayer antiskyrmions. (a) Illustration of an antiskyrmion-antiskyrmion pair in a trilayer structure. (b) The velocities of the antiskyrmion-antiskyrmion pair as a function of the driven current when $A_{\text{inter}} = -0.02 \text{ pJ m}^{-1}$. The SOT-induced propagation of the antiskyrmion-antiskyrmion pair at (c) decoupling strength $A_{\text{inter}} = -0.01 \text{ pJ m}^{-1}$ and (d) coupling strength $A_{\text{inter}} = -0.02 \text{ pJ m}^{-1}$. In the simulations, we adopt the following parameters: $A = 15 \text{ pJ m}^{-1}$, $K = 0.8 \text{ MJ m}^{-3}$, $M_s = 580 \text{ kA m}^{-1}$, $\alpha = 0.1$, and $P = 0.4$. The mesh size is $1 \times 1 \times 1 \text{ nm}^3$.

the AFM antiskyrmion (antiskyrmionium) by a large current causes a continuous stretching of the antiskyrmion (antiskyrmionium) along the transverse direction, eventually reaching the edges of the racetrack. On the other hand, the increasing components of the dissipative tensor \mathbf{D} and the vector \mathbf{u} , which are determined by the magnetic structures, also demonstrate the deformations of the AFM antiskyrmion and antiskyrmionium, as shown in Figs. 6(c) and 6(d). At a current density of 50 MA cm^{-2} for the AFM antiskyrmion and 30 MA cm^{-2} for the AFM antiskyrmionium, the components of the dissipative tensor \mathbf{D} and the vector \mathbf{u} correspond to the analytical solutions since the structures move along the track without deformation, appearing as rigid structures. However, a further increase in current causes the components to deviate increasingly from the analytical values, leading to velocities of the AFM antiskyrmion and antiskyrmionium that differ from the analytical solutions.

VI. SYNTHETIC ANTIFERROMAGNETIC ANTISKYRMION IN A BILAYER SYSTEM

A ferromagnetically coupled skyrmion-antiskyrmion pair was proposed in some theoretical and experimental works [9,17]. Because of their opposite topological charges, the skyrmion-antiskyrmion pair has no skyrmion Hall effect. Similar to bilayer skyrmions with antiferromagnetic coupling, the bilayer antiskyrmions shown in Fig. 7(a) have no transverse motion. The synthetic antiferromagnetic track is composed of two FM layers with one nonmagnetic spacer.

To simulate the current-driven motion of bilayer antiskyrmions, we consider a 256 nm long, 128 nm wide trilayer track, and the thicknesses of the top layer, spacer layer, and bottom layer are all 1.0 nm . The anisotropic DMI is set to

$D_x = -D_y = 3.5 \text{ mJ m}^{-2}$. When coupled by interfacial antiferromagnetic exchange interaction across the spacer layer, the antiskyrmions in the top and bottom layers can be stabilized in the track. We explicitly take into account the magnetic dipolar interaction. Figure 7(b) shows the relation between the current and velocity of the bilayer antiskyrmions when the exchange coupling is -0.02 pJ m^{-1} . Coupled with this strength, the antiskyrmions in the top and bottom layers are bound strongly. The antiskyrmions have the same speeds when driven by the SOT and STT. The efficiency of the SOT in driving the bilayer antiskyrmions is better than that of the STT. Figure 7(c) shows the trajectory of the bilayer antiskyrmions when the current density is $j = 5 \text{ MA cm}^{-2}$. With weak interlayer coupling $A_{\text{inter}} = -0.01 \text{ pJ m}^{-1}$, the antiskyrmions in the top and bottom layers move along the track with opposite transverse motions due to the opposite topological charges, leading to the destruction of the antiskyrmions in both layers when they touch the edges of the track, as shown in the decoupled case in Fig. 7(c). When the interfacial exchange coupling is strong enough, i.e., $A_{\text{inter}} = -0.02 \text{ pJ m}^{-1}$, the bilayer antiskyrmions are strongly bound. There is no skyrmion Hall effect with sufficient interfacial AFM exchange coupling because the Magnus forces acting on the top and the bottom antiskyrmions are exactly canceled, as shown in Fig. 7(d).

VII. CONCLUSION

In conclusion, our study systematically investigated the current-induced dynamics of the AFM antiskyrmion and antiskyrmionium. We found that the AFM antiskyrmion and antiskyrmionium can be created by the spin current in a designed geometry and can be stabilized in nanodisks in the presence of anisotropic DMI. The current-driven propagation of the AFM antiskyrmion and antiskyrmionium shows no transverse motion. Moreover, the velocities of the AFM antiskyrmion and antiskyrmionium differ due to the magnetization distributions for the SOT-induced motion but are identical for the STT-induced motion. The comparison of AFM and FM antiskyrmions (antiskyrmioniums) revealed several advantages of the former, including the absence of transverse motion and higher moving velocities. Especially, the critical driving current of the AFM antiskyrmion is about 37 times larger than that of the FM antiskyrmion, and AFM antiskyrmionium is more robust than the FM antiskyrmionium under high current densities. Additionally, we proposed antiferromagnetically coupled antiskyrmion-antiskyrmion pairs in a bilayer structure where the skyrmion Hall effect can be suppressed. Our findings offer promising potential for future spintronic devices with the current-driven dynamics of the AFM antiskyrmion and antiskyrmionium.

ACKNOWLEDGMENTS

The work is supported by the Guangdong Basic and Applied Basic Research Foundation (Grant No. 2021B1515120047), Guangdong Special Support Project (Grant No. 2019BT02X030), Shenzhen Fundamental Research Fund (Grant No. JCYJ20210324120213037), Shenzhen Peacock Group Plan (Grant No. KQTD20180413181702403), and National

Natural Science Foundation of China (NSFC; Grant No. 11974298). M.E. acknowledges the support from CREST, JST (Grant No. JPMJCR20T2).

APPENDIX: ANALYTICAL DERIVATION OF THE MOTION EQUATIONS

To derive the motion equation of magnetization in a two-sublattice antiferromagnetic system, we consider the dynamics of the total magnetization vector $\mathbf{m} = (\mathbf{s}_{i+1,j}^A + \mathbf{s}_{i,j}^B)/2$ and the Néel vector $\mathbf{n} = (\mathbf{s}_{i+1,j}^A - \mathbf{s}_{i,j}^B)/2$, where $\mathbf{s}_{i,j}^\tau$ is the unit magnetic moment with sublattice parameters $\tau = A, B$ and sublattice site (i, j) . Considering the antiferromagnetic exchange interaction is significantly strong in realistic cases, $\mathbf{m}^2 \ll \mathbf{n}^2 \sim 1$. The total magnetization \mathbf{m} and the Néel vector \mathbf{n} obey the following coupled equations:

$$\dot{\mathbf{n}} = (\gamma \mathbf{f}_m - \alpha \dot{\mathbf{m}}) \times \mathbf{n} + \mathbf{T}_{n,\text{SOT}} + \mathbf{T}_{n,\text{STT}}, \quad (\text{A1a})$$

$$\dot{\mathbf{m}} = (\gamma \mathbf{f}_n - \alpha \dot{\mathbf{n}}) \times \mathbf{n} + \mathbf{T}_{nl} + \mathbf{T}_{m,\text{SOT}} + \mathbf{T}_{m,\text{STT}}, \quad (\text{A1b})$$

where $\mathbf{f}_m = -\delta E/(\mu_0 M_s \delta \mathbf{m})$ and $\mathbf{f}_n = -\delta E/(\mu_0 M_s \delta \mathbf{n})$ are the effective fields associated with various energies in the system. $\mathbf{T}_{nl} = (\gamma \mathbf{f}_m - \alpha \dot{\mathbf{m}}) \times \mathbf{m}$ is the simplest non-linear term. We disregard such a higher-order term in the following. $\mathbf{T}_{n,\text{SOT}} = \gamma H_d \mathbf{m} \times \mathbf{p} \times \mathbf{n}$ and $\mathbf{T}_{m,\text{SOT}} = \gamma H_d \mathbf{n} \times \mathbf{p} \times \mathbf{n}$ are dampinglike spin-orbit torques (SOTs), with $H_d = j\hbar\theta_{\text{SH}}/(2\mu_0 e M_s t_z)$. $\mathbf{T}_{n,\text{STT}} = \gamma \eta (\mathbf{J} \cdot \nabla) \mathbf{n}$ and $\mathbf{T}_{m,\text{STT}} = \gamma \beta (\mathbf{J} \cdot \nabla) \mathbf{n} \times \mathbf{n}$ are spin transfer torques (STTs), with $\eta(\beta)$ being the adiabatic (nonadiabatic) parameter.

From Eq. (1), we can get the effective fields,

$$\mathbf{f}_m = -\frac{\lambda}{\mu_0 M_s} \mathbf{m} - \frac{L}{\mu_0 M_s} (\partial_x \mathbf{n} + \partial_y \mathbf{n}), \quad (\text{A2})$$

$$\begin{aligned} \mathbf{f}_n = & \frac{L}{\mu_0 M_s} (\partial_x \mathbf{m} + \partial_y \mathbf{m}) + \frac{A}{\mu_0 M_s} (\Delta \mathbf{n} + \partial_{xy} \mathbf{n}) + \frac{K}{\mu_0 M_s} n_z \mathbf{e}_z \\ & + \frac{D}{\mu_0 M_s} [\partial_x n_z \mathbf{e}_x + \partial_y n_z \mathbf{e}_y - (\partial_x n_x + \partial_y n_y) \mathbf{e}_z]. \end{aligned} \quad (\text{A3})$$

Here, we consider that $D_x = -D_y = D$.

Substituting Eq. (A2) into Eq. (A1a), we obtain the total magnetization,

$$\mathbf{m} = \frac{\mu_0 M_s}{\gamma \lambda} \dot{\mathbf{n}} \times \mathbf{n} - \frac{L}{\lambda} (\partial_x \mathbf{n} + \partial_y \mathbf{n}), \quad (\text{A4})$$

where only the leading terms are kept. Equation (A4) shows that the total magnetization depends on the spatial variation of the Néel vector. From Eqs. (A4) and (A3), we find the effective fields \mathbf{f}_n ,

$$\mathbf{f}_n = \frac{L}{\gamma \lambda} (\partial_i \dot{\mathbf{n}} \times \mathbf{n} + \dot{\mathbf{n}} \times \partial_i \mathbf{n}) + \mathbf{f}_n^*, \quad (\text{A5})$$

where

$$\begin{aligned} \mathbf{f}_n^* = & \frac{A^*}{\mu_0 M_s} (\partial_{xx} + \partial_{yy}) \mathbf{n} + \frac{K}{\mu_0 M_s} n_z \mathbf{e}_z \\ & + \frac{D}{\mu_0 M_s} [\partial_x n_z \mathbf{e}_x + \partial_y n_z \mathbf{e}_y - (\partial_x n_x + \partial_y n_y) \mathbf{e}_z], \end{aligned} \quad (\text{A6})$$

with $A^* = A/2$. On the other hand, from Eqs. (A1b) and (A4), we obtain

$$\frac{\mu_0 M_s}{\gamma \lambda} \ddot{\mathbf{n}} \times \mathbf{n} - \frac{L}{\lambda} \partial_i \ddot{\mathbf{n}} = (\gamma \mathbf{f}_n - \alpha \dot{\mathbf{n}}) \times \mathbf{n} + \mathbf{T}_{m,\text{SOT}} + \mathbf{T}_{m,\text{STT}}. \quad (\text{A7})$$

Substituting Eq. (A5) into Eq. (A7), we can get an equation that contains only the Néel vector \mathbf{n} ,

$$\begin{aligned} & \frac{\mu_0 M_s}{\gamma \lambda} \ddot{\mathbf{n}} \times \mathbf{n} - \frac{L}{\lambda} \partial_i \ddot{\mathbf{n}} \\ & = \frac{L}{\lambda} (\partial_i \dot{\mathbf{n}} \times \mathbf{n} + \dot{\mathbf{n}} \times \partial_i \mathbf{n}) \times \mathbf{n} \\ & \quad + \gamma \mathbf{f}_n^* \times \mathbf{n} - \alpha \dot{\mathbf{n}} \times \mathbf{n} + \mathbf{T}_{m,\text{SOT}} + \mathbf{T}_{m,\text{STT}}. \end{aligned} \quad (\text{A8})$$

Then, taking the cross product of Eq. (A8) with \mathbf{n} and ignoring the higher-order terms, we obtain

$$\begin{aligned} & \frac{\mu_0 M_s}{\gamma \lambda} \ddot{\mathbf{n}} \times \mathbf{n} \times \mathbf{n} = \gamma \mathbf{f}_n^* \times \mathbf{n} \times \mathbf{n} + \alpha \dot{\mathbf{n}} - \gamma H_d \mathbf{n} \times \mathbf{p} \\ & \quad - \gamma \beta (\mathbf{J} \cdot \nabla) \mathbf{n}. \end{aligned} \quad (\text{A9})$$

Using the scalar product in Eq. (A9) with $\mu_0 M_s \partial_i \mathbf{n}$ and integrating over the space, the Thiele equation is written as

$$\mathbf{a} \cdot \mathbf{M}_{\text{eff}} = \mathbf{F}_\alpha + \mathbf{F}_{\text{SOT}} + \mathbf{F}_{\text{STT}}, \quad (\text{A10})$$

where \mathbf{a} is the acceleration and \mathbf{M}_{eff} is the effective mass, which is defined as $\mu_0^2 M_s^2 t_z \mathbf{D} / \gamma^2 \lambda$. The first term on the right side of Eq. (A10) is the dissipative force, $\mathbf{F}_\alpha = -\alpha \mu_0 M_s t_z \mathbf{v} \cdot \mathbf{D} / \gamma$, where the dissipative tensor \mathbf{D} is given by $\mathbf{D} = \begin{pmatrix} d_{xx} & d_{xy} \\ d_{yx} & d_{yy} \end{pmatrix}$, with $d_{ij} = \delta_{ij} d = \int dxdy (\partial_i \mathbf{n} \cdot \partial_j \mathbf{n})$. The second and third terms on the right side of Eq. (A10) are the forces induced by the SOT and STT, respectively. Considering the current is applied along the x direction, they are written as

$$\mathbf{F}_{\text{SOT}} = \mathbf{F}_{\text{SOT},x} \mathbf{e}_x + \mathbf{F}_{\text{SOT},y} \mathbf{e}_y, \quad (\text{A11a})$$

$$\mathbf{F}_{\text{STT}} = -\mu_0 M_s t_z d \beta j \mathbf{e}_x. \quad (\text{A11b})$$

Here, $F_{\text{SOT},i} = -\mu_0 M_s t_z H_d u_i$, with

$$u_i = \int dxdy [(\mathbf{n} \times \mathbf{p}) \cdot \partial_i \mathbf{n}]. \quad (\text{A12})$$

For a centrosymmetric magnetic soliton, the order parameter \mathbf{n} is described by $\mathbf{n} = [\sin \theta(r) \cos \phi(\varphi), \sin \theta(r) \sin \phi(\varphi), \cos \theta(r)]$ in polar coordinates (r, φ) . Specifically, for a Néel-type antiskyrmion (antiskyrmionium), $\phi = -\varphi$. Considering $\mathbf{p} = -\mathbf{e}_y$, we can rewrite the tensor \mathbf{D} and the vector \mathbf{u} in polar coordinates,

$$d_{ij} = \delta_{ij} d = \delta_{ij} \pi \int \theta_r^2 + \sin^2 \theta / r^2 r dr, \quad (\text{A13a})$$

$$u_x = \int \left[\cos^2 \varphi \frac{d\theta}{dr} + \frac{1}{2r} \sin 2\theta \sin^2 \varphi \right] r dr d\varphi, \quad (\text{A13b})$$

$$u_y = \int \left[\frac{\sin 2\varphi}{2} \left(\frac{d\theta}{dr} - \frac{\sin 2\theta}{2r} \right) \right] r dr d\varphi. \quad (\text{A13c})$$

In general, the steady motion velocity is given by the following matrix:

$$\begin{pmatrix} v_x \\ v_y \end{pmatrix} = \frac{\gamma H_d}{\alpha d} \begin{pmatrix} u_x \\ u_y \end{pmatrix} + \frac{\gamma \beta j}{\alpha} \begin{pmatrix} e_x \\ 0 \end{pmatrix}. \quad (\text{A14})$$

Therefore, we can find that the velocity of a Néel-type antiskyrmion (antiskyrmionium) depends on the internal spin distribution.

-
- [1] N. Nagaosa and Y. Tokura, *Nat. Nanotechnol.* **8**, 899 (2013).
- [2] X. Zhang, M. Ezawa, and Y. Zhou, *Sci. Rep.* **5**, 9400 (2015).
- [3] X. Zhang, Y. Zhou, K. Mee Song, T.-E. Park, J. Xia, M. Ezawa, X. Liu, W. Zhao, G. Zhao, and S. Woo, *J. Phys.: Condens. Matter* **32**, 143001 (2020).
- [4] J. Sampaio, V. Cros, S. Rohart, A. Thiaville, and A. Fert, *Nat. Nanotechnol.* **8**, 839 (2013).
- [5] K. M. Song, J.-S. Jeong, B. Pan, X. Zhang, J. Xia, S. Cha, T.-E. Park, K. Kim, S. Finizio, J. Raabe, J. Chang, Y. Zhou, W. Zhao, W. Kang, H. Ju, and S. Woo, *Nat. Electron.* **3**, 148 (2020).
- [6] A. A. Kovalev and S. Sandhoefner, *Front. Phys.* **6**, 98 (2018).
- [7] W. Koshibae and N. Nagaosa, *Nat. Commun.* **7**, 10542 (2016).
- [8] M. Hoffmann, G. P. Müller, C. Melcher, and S. Blügel, *Front. Phys.* **9**, 769873 (2021).
- [9] R. C. Silva, R. L. Silva, and A. R. Pereira, *J. Phys.: Condens. Matter* **33**, 105802 (2021).
- [10] I. Dzyaloshinsky, *J. Phys. Chem. Solids* **4**, 241 (1958).
- [11] T. Moriya, *Phys. Rev.* **120**, 91 (1960).
- [12] X. Z. Yu, Y. Onose, N. Kanazawa, J. H. Park, J. H. Han, Y. Matsui, N. Nagaosa, and Y. Tokura, *Nature (London)* **465**, 901 (2010).
- [13] S. Woo, K. Litzius, B. Krüger, M.-Y. Im, L. Caretta, K. Richter, M. Mann, A. Krone, R. M. Reeve, M. Weigand, P. Agrawal, I. Lemesch, M.-A. Mawass, P. Fischer, M. Kläui, and G. S. D. Beach, *Nat. Mater.* **15**, 501 (2016).
- [14] W. Jiang, X. Zhang, G. Yu, W. Zhang, X. Wang, M. B. Jungfleisch, J. Pearson, X. Cheng, O. Heinonen, K. L. Wang, Y. Zhou, A. Hoffmann, and S. G. E. te Velthuis, *Nat. Phys.* **13**, 162 (2017).
- [15] X. Z. Yu, N. Kanazawa, W. Z. Zhang, T. Nagai, T. Hara, K. Kimoto, Y. Matsui, Y. Onose, and Y. Tokura, *Nat. Commun.* **3**, 988 (2012).
- [16] G. Yu, P. Upadhyaya, X. Li, W. Li, S. K. Kim, Y. Fan, K. L. Wong, Y. Tserkovnyak, P. K. Amiri, and K. L. Wang, *Nano Lett.* **16**, 1981 (2016).
- [17] S. Huang, C. Zhou, G. Chen, H. Shen, A. K. Schmid, K. Liu, and Y. Wu, *Phys. Rev. B* **96**, 144412 (2017).
- [18] L. Camosi, N. Rougemaille, O. Fruchart, J. Vogel, and S. Rohart, *Phys. Rev. B* **97**, 134404 (2018).
- [19] L. Peng, K. V. Iakoubovskii, K. Karube, Y. Taguchi, Y. Tokura, and X. Yu, *Adv. Sci.* **9**, 2202950 (2022).
- [20] L. Peng, R. Takagi, W. Koshibae, K. Shibata, K. Nakajima, T. H. Arima, N. Nagaosa, S. Seki, X. Yu, and Y. Tokura, *Nat. Nanotechnol.* **15**, 181 (2020).
- [21] S. Jamaluddin, S. K. Manna, B. Giri, P. V. P. Madduri, S. S. P. Parkin, and A. K. Nayak, *Adv. Funct. Mater.* **29**, 1901776 (2019).
- [22] A. K. Nayak, V. Kumar, T. Ma, P. Werner, E. Pippel, R. Sahoo, F. Damay, U. K. Rossler, C. Felser, and S. S. P. Parkin, *Nature (London)* **548**, 561 (2017).
- [23] K. Karube, L. Peng, J. Masell, X. Yu, F. Kagawa, Y. Tokura, and Y. Taguchi, *Nat. Mater.* **20**, 335 (2021).
- [24] K. Karube, L. Peng, J. Masell, M. Hemmida, H.-A. Krug von Nidda, I. Kézsmárki, X. Yu, Y. Tokura, and Y. Taguchi, *Adv. Mater.* **34**, 2108770 (2022).
- [25] A. N. Bogdanov and D. A. Yablonskii, *Zh. Eksp. Teor. Fiz.* **95**(1), 178 (1989).
- [26] J. Jena, R. Stinshoff, R. Saha, A. K. Srivastava, T. Ma, H. Deniz, P. Werner, C. Felser, and S. S. P. Parkin, *Nano Lett.* **20**, 59 (2020).
- [27] T. Ma, A. K. Sharma, R. Saha, A. K. Srivastava, P. Werner, P. Vir, V. Kumar, C. Felser, and S. S. P. Parkin, *Adv. Mater.* **32**, 2002043 (2020).
- [28] M. Hoffmann, B. Zimmermann, G. P. Müller, D. Schürhoff, N. S. Kiselev, C. Melcher, and S. Blügel, *Nat. Commun.* **8**, 308 (2017).
- [29] L. Camosi, S. Rohart, O. Fruchart, S. Pizzini, M. Belmeguenai, Y. Roussigné, A. Stashkevich, S. M. Cherif, L. Ranno, M. de Santis, and J. Vogel, *Phys. Rev. B* **95**, 214422 (2017).
- [30] U. Güngördü, R. Nepal, O. A. Tretiakov, K. Belashchenko, and A. A. Kovalev, *Phys. Rev. B* **93**, 064428 (2016).
- [31] B. Dupé, C. N. Kruse, T. Dornheim, and S. Heinze, *New J. Phys.* **18**, 055015 (2016).
- [32] L. Desplat, J.-V. Kim, and R. L. Stamps, *Phys. Rev. B* **99**, 174409 (2019).
- [33] A. O. Leonov and M. Mostovoy, *Nat. Commun.* **6**, 8275 (2015).
- [34] V. Lohani, C. Hickey, J. Masell, and A. Rosch, *Phys. Rev. X* **9**, 041063 (2019).
- [35] X. Zhang, J. Xia, Y. Zhou, X. Liu, H. Zhang, and M. Ezawa, *Nat. Commun.* **8**, 1717 (2017).
- [36] W. Koshibae and N. Nagaosa, *Nat. Commun.* **5**, 5148 (2014).
- [37] S. Kandukuri, V. S. N. Murthy, and P. K. Thiruvikraman, *Sci. Rep.* **11**, 18945 (2021).
- [38] P. Siegl, M. Stier, A. F. Schäffer, E. Y. Vedmedenko, T. Posske, R. Wiesendanger, and M. Thorwart, *Phys. Rev. B* **106**, 014421 (2022).
- [39] S. Zhang, A. K. Petford-Long, and C. Phatak, *Sci. Rep.* **6**, 31248 (2016).
- [40] D. A. Kitchaev and A. Van der Ven, *Phys. Rev. Mater.* **5**, 124408 (2021).
- [41] S. Sandhoefner, A. Raeliarijaona, R. Nepal, D. Snyder-Tinoco, and A. A. Kovalev, *Phys. Rev. B* **104**, 064417 (2021).
- [42] C. Song, C. Jin, H. Xia, J. Wang, Y. Ma, J. Wang, and Q. Liu, *arXiv:1810.02464*.
- [43] X. Zhang, G. P. Zhao, H. Fangohr, J. P. Liu, W. X. Xia, J. Xia, and F. J. Morvan, *Sci. Rep.* **5**, 7643 (2015).
- [44] M. Stier, W. Hausler, T. Posske, G. Gurski, and M. Thorwart, *Phys. Rev. Lett.* **118**, 267203 (2017).
- [45] S. K. Panigrahy, C. Singh, and A. K. Nayak, *Appl. Phys. Lett.* **115**, 182403 (2019).
- [46] L. Shen, X. Li, Y. Zhao, J. Xia, G. Zhao, and Y. Zhou, *Phys. Rev. Appl.* **12**, 064033 (2019).

- [47] X. Liang, J. Xia, X. Zhang, M. Ezawa, O. A. Tretiakov, X. Liu, L. Qiu, G. Zhao, and Y. Zhou, *Appl. Phys. Lett.* **119**, 062403 (2021).
- [48] X. C. Zhang, Y. Zhou, and M. Ezawa, *Sci. Rep.* **6**, 24795 (2016).
- [49] X. C. Zhang, Y. Zhou, and M. Ezawa, *Nat. Commun.* **7**, 10293 (2016).
- [50] X. G. Li, L. C. Shen, Y. H. Bai, J. L. Wang, X. C. Zhang, J. Xia, M. Ezawa, O. A. Tretiakov, X. H. Xu, M. Mruczkiewicz, M. Krawczyk, Y. B. Xu, R. F. L. Evans, R. W. Chantrell, and Y. Zhou, *npj Comput. Mater.* **6**, 169 (2020).
- [51] V. Baltz, A. Manchon, M. Tsoi, T. Moriyama, T. Ono, and Y. Tserkovnyak, *Rev. Mod. Phys.* **90**, 015005 (2018).
- [52] O. Gomonay, V. Baltz, A. Brataas, and Y. Tserkovnyak, *Nat. Phys.* **14**, 213 (2018).
- [53] J. Barker and O. A. Tretiakov, *Phys. Rev. Lett.* **116**, 147203 (2016).
- [54] L. Shen, J. Xia, X. Zhang, M. Ezawa, O. A. Tretiakov, X. Liu, G. Zhao, and Y. Zhou, *Phys. Rev. Lett.* **124**, 037202 (2020).
- [55] A. N. Bogdanov, U. K. Röbber, M. Wolf, and K.-H. Müller, *Phys. Rev. B* **66**, 214410 (2002).
- [56] A. Zheludev, G. Shirane, Y. Sasago, N. Kiode, and K. Uchinokura, *Phys. Rev. B* **54**, 15163 (1996).
- [57] A. Zheludev, S. Maslov, G. Shirane, Y. Sasago, N. Koide, and K. Uchinokura, *Phys. Rev. Lett.* **78**, 4857 (1997).
- [58] M. D. Lumsden, B. C. Sales, D. Mandrus, S. E. Nagler, and J. R. Thompson, *Phys. Rev. Lett.* **86**, 159 (2001).
- [59] A. Mukherjee, D. S. Kathyat, and S. Kumar, *Phys. Rev. B* **105**, 075102 (2022).
- [60] E. G. Tveten, T. Müller, J. Linder, and A. Brataas, *Phys. Rev. B* **93**, 104408 (2016).
- [61] E. G. Tveten, A. Qaiumzadeh, O. A. Tretiakov, and A. Brataas, *Phys. Rev. Lett.* **110**, 127208 (2013).
- [62] A. Vansteenkiste, J. Leliaert, M. Dvornik, M. Helsen, F. Garcia-Sanchez, and B. Van Waeyenberge, *AIP Adv.* **4**, 107133 (2014).
- [63] A. A. Thiele, *Phys. Rev. Lett.* **30**, 230 (1973).
- [64] O. A. Tretiakov, D. Clarke, G.-W. Chern, Y. B. Bazaliy, and O. Tchernyshyov, *Phys. Rev. Lett.* **100**, 127204 (2008).
- [65] See Supplemental Material at <http://link.aps.org/supplemental/10.1103/PhysRevB.107.174409> for movies showing the creation processes of an AFM antiskyrmion and an AFM antiskyrmionium.
- [66] J. Xia, X. Zhang, M. Ezawa, Q. Shao, X. Liu, and Y. Zhou, *Appl. Phys. Lett.* **116**, 022407 (2020).
- [67] S. Rohart and A. Thiaville, *Phys. Rev. B* **88**, 184422 (2013).
- [68] J. Mulkers, M. V. Milošević, and B. Van Waeyenberge, *Phys. Rev. B* **93**, 214405 (2016).
- [69] S. Komineas and N. Papanicolaou, *Phys. Rev. B* **92**, 174405 (2015).
- [70] E. A. Tremsina and G. S. D. Beach, *Phys. Rev. B* **106**, L220402 (2022).
- [71] C. Jin, C. Song, J. Wang, and Q. Liu, *Appl. Phys. Lett.* **109**, 182404 (2016).
- [72] S. Komineas and N. Papanicolaou, *SciPost Phys.* **8**, 086 (2020).
- [73] A. Salimath, F. Zhuo, R. Tomasello, G. Finocchio, and A. Manchon, *Phys. Rev. B* **101**, 024429 (2020).
- [74] X. Zhang, J. Xia, Y. Zhou, D. Wang, X. Liu, W. Zhao, and M. Ezawa, *Phys. Rev. B* **94**, 094420 (2016).
- [75] X. Liang, X. Zhang, L. Shen, J. Xia, M. Ezawa, X. Liu, and Y. Zhou, *Phys. Rev. B* **104**, 174421 (2021).